ALMA MATER STUDIORUM · UNIVERSITÀ DI BOLOGNA

School of Science
Department of Physics and Astronomy
Bachelor's Degree in Physics

Measurement of $K^-\pi^+$ detection asymmetry with LHCb Run 3 data

Supervisor:
Dr. Fabio Ferrari

Co-supervisor:
Dr. Angelo Carbone

Submitted by:
Egidio Romano

Academic Year 2025/2026

Abstract

This thesis presents the determination of the detection asymmetry $A_{\text{det}}(K^-\pi^+)$ for the $K^-\pi^+$ pair using data collected by the LHCb experiment during the 2024 Run 3 at a centre-of-mass energy of 13.6 TeV. The analysis is based on the decay channels $D^+ \to K^-\pi^+\pi^+$ and $D^+ \to K^0_S\pi^+$. The signal is modelled by a Johnson S_U distribution plus two Gaussian functions with a common mean, while the background is described by an exponential function. Raw asymmetries are extracted from simultaneous fits to the invariant mass distributions of D^+ and D^- candidates for each channel and magnet polarity. Subtracting the raw asymmetries of the two channels, the detection asymmetry $A_{\text{det}}(K^-\pi^+)$ is obtained:

$$A_{\text{det}}(K^-\pi^+) = (-0.95 \pm 0.03) \times 10^{-2}.$$

The measurement provides a crucial input for the determination of production asymmetries and for future studies of CP violation in the charm sector. It will be completed with a detailed study of systematic uncertainties within the Bologna LHCb group.

Contents

1 Theoretical Framework **4**

1.1 The standard model 4

1.1.1 Helicity and Chirality 7

1.2 Discrete symmetry transformations 7

1.2.1 Charge conjugation transformation 8

1.2.2 Parity Transformation 8

1.2.3 CP transformation 9

1.3 Quark flavour mixing 10

1.4 CP Violation in mesons systems 12

1.4.1 Detection asymmetry for $K\pi$ pairs 14

2 The LHCb experiment **15**

2.1 LHCb detector layout 16

2.1.1 The Vertex Locator (VELO) 18

2.1.2 Upstream tracker (UT) and Scintillating Fibres (SciFi) tracker . . . 19

2.1.3 The Dipole Magnet 20

2.2 Particle identification systems 22

2.2.1 Principle of Cherenkov detection 22

2.2.2 RICH1 and RICH2 23

2.3 Calorimeter System 24

2.4 Muon System 25

2.5 Trigger and Data Acquisition System 26

2.6 Detector Induced Asymmetries 26

3 Measurement of the $K^-\pi^+$ detection asymmetry **28**

3.1 Motivation and observable definition 28

3.2 Choice of control channels 28

3.3 Decomposition of the raw asymmetry 29

3.4 Experimental procedure overview 30

3.5 Fit model 31

3.6 Results of the fits 32

3.7 Combination of magnet polarities 35
3.8 Final detection asymmetry 35

Conclusions **36**

Chapter 1

Theoretical Framework

1.1 The standard model

In 1954 Chen Ning Yang and Robert Mills transformed theoretical physics by extending the concept of local gauge transformations to non-Abelian symmetry groups[1]. This shift from a simple $U(1)$ gauge symmetry[1] to a non-Abelian $SU(2)$ symmetry laid the foundation for the entire Standard Model of particle physics. Despite initial challenges (such as the apparent masslessness of the resulting force mediators), this framework provided the essential breakthrough for modern particle physics establishing gauge theory as the universal language for describing the strong, weak, and electromagnetic interactions. Today, the Standard Model (SM) represents the reference theory for elementary particle physics[2]. The underlying mathematical language is quantum field theory (QFT), a formalism in which elementary particles are described as quantum excitations of underlying fields and interactions are interpreted as exchanges of mediator particles: gauge bosons[3]. The local symmetry group on which the entire SM is based is given by:

$$G_{SM} = SU(3)_C \otimes SU(2)_L \otimes U(1)_Y. \tag{1.1}$$

Here, each subgroup governs a specific interaction. In particular, $SU(3)_C$ is the gauge group of color transformations describing the strong force. Its mediators, the gluons, are massless gauge bosons that possess a color charge themselves (a property that enables their self-interaction and gives rise to fundamental phenomena such as quark confinement and asymptotic freedom [1]). The electroweak sector, instead, is based on the gauge group $SU(2)_L \otimes U(1)_Y$. The subscript L emphasizes that only left-handed fermions transform non-trivially under $SU(2)_L$. Left-handed fields are arranged in weak isospin doublets, while right-handed fields are $SU(2)_L$ singlets. Their field content is therefore given by[5]:

[1] $\mathrm{U}(1)$ is the Abelian gauge group of quantum electrodynamics (QED). Mathematically representing phase rotations on the complex unit circle, its local invariance dictates the existence of the electromagnetic field, whose quantum mediator (the photon) is uncharged and non-self-interacting.

$$q_L^i = \begin{pmatrix} u \\ d \end{pmatrix}_L, \begin{pmatrix} c \\ s \end{pmatrix}_L, \begin{pmatrix} t \\ b \end{pmatrix}_L, \qquad L_L^i = \begin{pmatrix} \nu_e \\ e \end{pmatrix}_L, \begin{pmatrix} \nu_\mu \\ \mu \end{pmatrix}_L, \begin{pmatrix} \nu_\tau \\ \tau \end{pmatrix}_L, \tag{1.2}$$

$$u_R^i = (u_R,\ c_R,\ t_R), \qquad d_R^i = (d_R,\ s_R,\ b_R), \qquad e_R^i = (e_R,\ \mu_R,\ \tau_R). \tag{1.3}$$

The electroweak representations of these fields are characterized by the weak isospin T_3 and the weak hypercharge Y, which are related to the electric charge through the Gell-Mann–Nishijima relation:

$$Q = T_3 + \frac{Y}{2}. \tag{1.4}$$

Hypercharge assignments distinguish the different fermionic representations. Left-handed quark doublets carry hypercharge $Y = 1/3$, while left-handed lepton doublets have $Y = -1$. Right-handed up-type quarks, down-type quarks, and charged leptons carry hypercharges $4/3$, $-2/3$, and -2, respectively [5]. The electroweak gauge fields consist of b_μ^1, b_μ^2, b_μ^3 for $SU(2)_L$ and a_μ for $U(1)_Y$. The physical charged gauge bosons are obtained as linear combinations of the $SU(2)_L$ gauge fields[5]:

$$W_\mu^\pm = \frac{b_\mu^1 \mp i b_\mu^2}{\sqrt{2}}. \tag{1.5}$$

In the neutral sector, b_μ^3 and a_μ mix to form the photon and the Z boson:

$$Z_\mu = \frac{-g' a_\mu + g b_\mu^3}{\sqrt{g^2 + g'^2}}, \qquad A_\mu = \frac{g a_\mu + g' b_\mu^3}{\sqrt{g^2 + g'^2}}. \tag{1.6}$$

Here g and g' denote the gauge couplings associated with $SU(2)_L$ and $U(1)_Y$ respectively. The orthogonality of these combinations ensures that A_μ remains massless and is identified with the photon, while Z_μ acquires a mass after electroweak symmetry breaking. This structure is conventionally parametrized in terms of the Weinberg angle θ_W, defined by $\tan\theta_W = g'/g$. The relation between weak isospin, hypercharge, and electric charge ensures the consistency of this construction. Since exact gauge symmetry forbids explicit mass terms for the gauge bosons, the Standard Model introduces a complex scalar field whose spontaneous symmetry breaking gives rise to the Brout–Englert–Higgs mechanism. The quantum excitation of this field corresponds to the Higgs boson (H) [6]. This mechanism generates the masses of the $W_\mu^\pm$ and Z_μ bosons while preserving the mathematical consistency and renormalizability of the theory. Through Yukawa couplings, it also provides masses to all massive fermions. The Standard Model (which had successfully predicted the charm, bottom, and top quarks as well as the $W_\mu^\pm$ and Z_μ bosons) was experimentally completed with the discovery of the Higgs boson at CERN in 2012 [7].

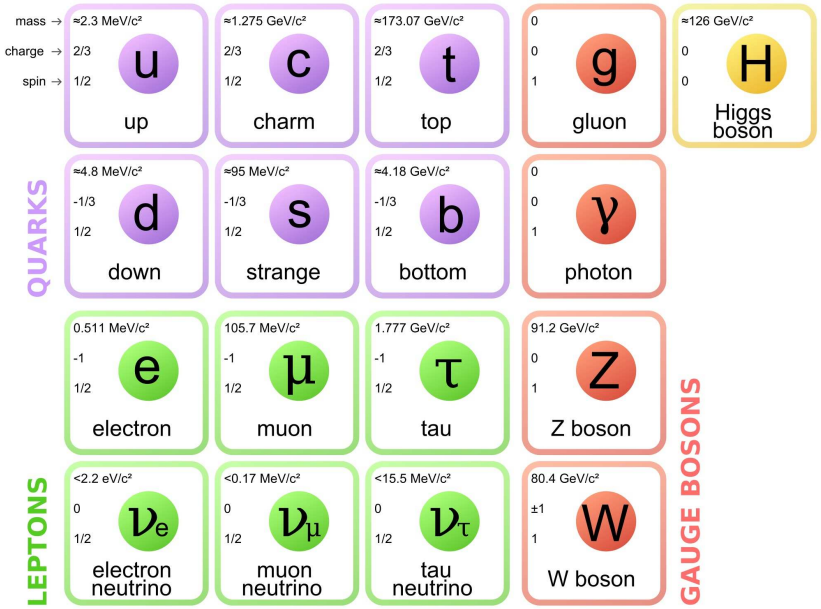

Figure 1.1: Particle content of the Standard Model (notation differs slightly from that used in the text).

The particle content of the Standard Model is summarized in Figure 1.1 (divided into two main categories: fermions and bosons). Fermions are grouped into:

- *quarks*, they carry fractional electric charges ($+2/3$ for up-type and $-1/3$ for down-type) and transform as triplets under $SU(3)_C$. As a consequence of color confinement, they are not observed as free particles but only in color-neutral bound states called hadrons (mesons and baryons);

- *leptons*, they consist of six flavors (electron, muon, tau, and their corresponding neutrinos). They are color singlets and therefore do not participate in the strong interaction. Charged leptons carry electric charge -1, while neutrinos are electrically neutral and have small but non-zero masses[2].

Each fermion has a corresponding antiparticle with the same mass and spin but opposite additive quantum numbers (such as electric charge and color charge).

The gauge bosons are:

- *photon*, the massless and electrically neutral mediator of the electromagnetic interaction;

- $W^{\pm}_{\mu}$, Z_{μ} *bosons*, the massive mediators of the weak interaction ($m_W \approx 80.4$ GeV/c^2, $m_Z \approx 91.2$ GeV/c^2) [2]. They mediate processes such as nuclear beta decay[3]. CP

[2]Neutrino oscillations, first observed in the late 1990s, provide direct evidence that neutrinos possess non-zero masses, contrary to the original Standard Model prediction[2].

[3]Nuclear β-decay is a weak interaction process in which an unstable nucleus transitions to a more energetically favorable isobar by converting a neutron into a proton (or vice versa), thereby adjusting its proton-to-neutron ratio. These processes are mediated by $W^{\pm}_{\mu}$ bosons, which induce flavor-changing transitions among quarks[2].

violation in weak charged-current interactions arises from the complex phase of the CKM matrix in the quark sector [1].

- *gluons*, eight massless gauge bosons of the $SU(3)_C$ color symmetry. The associated color charge generalizes the concept of electric charge in QED, existing in three types (red, green, and blue) together with their corresponding anticolors.

- *Higgs boson.*

1.1.1 Helicity and Chirality

To fully understand the chiral structure of weak interactions, it is necessary to define more precisely the notions of helicity and chirality, which distinguish left- and right-handed fermionic states. Helicity is defined as the projection of a particle's spin operator onto the direction of its momentum[4]:

$$h = \frac{\mathbf{S} \cdot \mathbf{p}}{|\mathbf{p}|} \tag{1.7}$$

It measures whether the spin is aligned or anti-aligned with the particle's direction of motion. Here $\mathbf{S}$ denotes the spin operator, while $\mathbf{p}$ is the momentum operator. The helicity operator corresponds to the component of the spin along the direction of motion, and its eigenstates describe states of definite handedness. For spin-$\frac{1}{2}$ particles, the helicity eigenvalues are $\pm\frac{1}{2}$ (in units of $\hbar$)[4]. Positive helicity states are referred to as right-handed, while negative helicity corresponds to left-handed states. For massless particles, helicity is Lorentz-invariant[5]. Chirality is a fundamental property of fermion fields defined through the γ^5 Dirac matrix ($\gamma^5 = i\gamma^0\gamma^1\gamma^2\gamma^3$). Any fermion field ψ can be decomposed into its chiral components using the projection operators P_L and P_R[3]:

$$\psi = \psi_L + \psi_R = \left(\frac{1-\gamma^5}{2}\right)\psi + \left(\frac{1+\gamma^5}{2}\right)\psi, \tag{1.8}$$

where ψ_L and ψ_R denote the left-handed and right-handed chiral components, respectively. For massless particles, chirality and helicity coincide: left-chiral states correspond to negative helicity and right-chiral states to positive helicity.

1.2 Discrete symmetry transformations

A fruitful approach in particle physics is to study how fundamental interactions behave under specific transformations of the dynamical variables on which they depend. Of particular

[4] In qualitative discussions helicity eigenvalues are often rescaled to ± 1 for convenience.

[5] For massive particles helicity is not Lorentz-invariant since a Lorentz boost can reverse the direction of momentum while leaving spin unchanged, thus flipping the helicity sign.

interest are those transformations that leave the interactions invariant, and are therefore referred to as symmetry transformations. In the present work, the symmetry of central relevance is CP, defined as the sequential composition of charge conjugation (C) and parity (P).

1.2.1 Charge conjugation transformation

Charge conjugation is an internal symmetry transformation acting on the quantum numbers of a system. Its effect consists of reversing additive quantum numbers such as electric charge, baryon number, and strangeness, while leaving spin unchanged. In essence, it maps a particle into its corresponding antiparticle. Following the formalism of quantum mechanics [8], every physical state is represented by a vector in a Hilbert space, denoted using bra-ket notation. When a system possesses additional degrees of freedom (such as spatial position $\mathbf{r}$, spin $\mathbf{s}$, and internal quantum numbers $\mathbf{q}$) the state is explicitly written as $|\psi(\mathbf{r}, \mathbf{s}, \mathbf{q})\rangle$. Formally, the charge conjugation transformation is represented by a unitary operator $\hat{C}$, acting on the state vector as follows:

$$\hat{C}|\psi(\mathbf{r}, \mathbf{s}, \mathbf{q})\rangle = |\psi(\mathbf{r}, \mathbf{s}, -\mathbf{q})\rangle. \tag{1.9}$$

A double application of $\hat{C}$ must return the original state:

$$\hat{C}^2|\psi(\mathbf{r}, \mathbf{s}, \mathbf{q})\rangle = \hat{C}|\psi(\mathbf{r}, \mathbf{s}, -\mathbf{q})\rangle = |\psi(\mathbf{r}, \mathbf{s}, \mathbf{q})\rangle, \tag{1.10}$$

which forces $\hat{C}^2 = \hat{\mathbb{I}}$. Consequently, the eigenvalues of $\hat{C}$ are ± 1. Only particles that coincide with their own antiparticles (such as the photon γ or the neutral pion π^0) can be eigenstates of $\hat{C}$. The weak interaction maximally violates C symmetry [9].

1.2.2 Parity Transformation

The parity transformation corresponds to the inversion of all spatial coordinates. A unitary parity operator $\hat{P}$ is defined, acting on a state $|\psi(\mathbf{r}, \mathbf{s}, \mathbf{q})\rangle$ as:

$$\hat{P}|\psi(\mathbf{r}, \mathbf{s}, \mathbf{q})\rangle = |\psi(-\mathbf{r}, \mathbf{s}, \mathbf{q})\rangle. \tag{1.11}$$

Since a double application of $\hat{P}$ restores the original configuration

$$\hat{P}^2|\psi(\mathbf{r}, \mathbf{s}, \mathbf{q})\rangle = \hat{P}|\psi(-\mathbf{r}, \mathbf{s}, \mathbf{q})\rangle = |\psi(\mathbf{r}, \mathbf{s}, \mathbf{q})\rangle, \tag{1.12}$$

it follows that $\hat{P}^2 = \hat{\mathbb{I}}$. The corresponding eigenvalue equation is therefore

$$\hat{P}|\psi(\mathbf{r}, \mathbf{s}, \mathbf{q})\rangle = \pm|\psi(\mathbf{r}, \mathbf{s}, \mathbf{q})\rangle \tag{1.13}$$

with eigenvalues restricted to ± 1. For particles at rest, parity becomes an intrinsic quantum number. Within the Dirac formalism, fermions and antifermions carry opposite intrinsic parity (up to a phase convention), whereas bosons and antibosons share the same intrinsic parity. In standard conventions, fermions are assigned positive intrinsic parity, while their antiparticles are assigned negative parity. States that are not eigenstates of $\hat{P}$ do not possess a well-defined parity. Parity conservation was long assumed to be a fundamental symmetry of nature, until it was experimentally disproved in weak-interaction processes, most notably in nuclear β-decay [10].

1.2.3 CP transformation

By 1957 parity (P) violation in weak interactions had been firmly established [10]. It was subsequently shown that charge conjugation (C) is also not conserved in weak processes, reflecting the chiral structure of the interaction, which couples only to left-handed particles and right-handed antiparticles. Despite this, the combined CP symmetry was initially expected to be conserved, since a CP transformation maps a left-handed neutrino into a right-handed antineutrino, which still participates in weak interactions. This expectation was overturned in 1964 by Cronin and Fitch through the observation of CP violation in the neutral kaon system K^0–$\bar{K}^0$ [11]. In the limit of exact CP invariance, the neutral kaon system can be expressed in terms of the eigenstates

$$\begin{aligned} |K_1\rangle &= \frac{1}{\sqrt{2}}\left(|K^0\rangle - |\bar{K}^0\rangle\right), \quad CP = +1, \\ |K_2\rangle &= \frac{1}{\sqrt{2}}\left(|K^0\rangle + |\bar{K}^0\rangle\right), \quad CP = -1. \end{aligned} \tag{1.14}$$

Under this assumption, the decay $K_2 \to 2\pi$ would be forbidden, so its observation provided direct evidence of CP violation. In reality, the physical states K_S and K_L are not pure CP eigenstates but superpositions:

$$\begin{aligned} |K_S\rangle &= \frac{1}{\sqrt{1+|\epsilon|^2}}\left(|K_1\rangle + \epsilon|K_2\rangle\right), \\ |K_L\rangle &= \frac{1}{\sqrt{1+|\epsilon|^2}}\left(|K_2\rangle + \epsilon|K_1\rangle\right). \end{aligned} \tag{1.15}$$

where the complex parameter $|\epsilon| \simeq 2.3 \times 10^{-3}$ quantifies indirect CP violation in the kaon system. CP violation can be classified into direct and indirect types: the former arises from differences in decay amplitudes between particles and antiparticles, while the latter originates from mixing between CP eigenstates [11]. Within the Standard Model, CP violation in the quark sector is ultimately encoded in a single irreducible complex phase of the Cabibbo–Kobayashi–Maskawa (CKM) matrix, which governs flavour mixing in weak charged-current interactions [6].

1.3 Quark flavour mixing

The physical relevance of quark flavour mixing becomes evident from a simple experimental observation: if all quark flavours were equally accessible through the strong interaction, the hadronic spectrum would contain more than one hundred stable (or strongly metastable) ground states. In contrast, ordinary matter is essentially built from only two light baryons: the proton, which is stable, and the neutron, which becomes stable only when bound inside nuclei [6]. The first systematic description of quark mixing dates back to the 1960s, when only three quark flavours were known (u, d, and s). In 1963, Nicola Cabibbo introduced a quantitative framework to describe the observed pattern of weak decays [6]. His key insight was that the weak-interaction eigenstates of down-type quarks do not coincide with their mass eigenstates. Instead, the weak states d' and s' are linear combinations of the mass eigenstates d and s, corresponding to a rotation in flavour space:

$$\begin{pmatrix} d' \\ s' \end{pmatrix} = \begin{pmatrix} \cos\theta_C & -\sin\theta_C \\ \sin\theta_C & \cos\theta_C \end{pmatrix} \begin{pmatrix} d \\ s \end{pmatrix} \tag{1.16}$$

This single-parameter mixing, governed by the Cabibbo angle θ_C, can be inferred experimentally from decay rates of pions and kaons, yielding $\theta_C \simeq 13^\circ$. Although highly successful in describing two-generation processes, the Cabibbo scheme proved insufficient when rarer weak decays were investigated. In particular, a 2×2 mixing structure could not naturally account for the strong suppression of flavour-changing neutral currents, such as $K^0 \to \mu^+\mu^-$, without additional assumptions. This limitation was resolved in 1973 by Kobayashi and Maskawa [2], who extended the formalism to three quark families, anticipating the existence of the charm, bottom, and top quarks. In this framework, quark mixing is described by a unitary 3×3 matrix, now known as the Cabibbo–Kobayashi–Maskawa matrix (CKM matrix):

$$V = \begin{pmatrix} V_{ud} & V_{us} & V_{ub} \\ V_{cd} & V_{cs} & V_{cb} \\ V_{td} & V_{ts} & V_{tb} \end{pmatrix} \tag{1.17}$$

This matrix connects the weak eigenstates of down-type quarks to their mass eigenstates through:

$$\begin{pmatrix} d' \\ s' \\ b' \end{pmatrix} = V \begin{pmatrix} d \\ s \\ b \end{pmatrix} \tag{1.18}$$

The introduction of three generations not only resolved the shortcomings of the Cabibbo model but also provided the necessary framework for CP violation in the Standard Model. The CKM matrix has then four degrees of freedom: three real angles θ_{12}, θ_{23}, θ_{13} and a phase δ. This allows the CKM matrix to be written as:

$$V = \begin{pmatrix} c_{12}c_{13} & s_{12}c_{13} & s_{13}e^{-i\delta} \\ -s_{12}c_{23} - c_{12}s_{23}s_{13}e^{i\delta} & c_{12}c_{23} - s_{12}s_{23}s_{13}e^{i\delta} & s_{23}c_{13} \\ s_{12}s_{23} - c_{12}c_{23}s_{13}e^{i\delta} & -c_{12}s_{23} - s_{12}c_{23}s_{13}e^{i\delta} & c_{23}c_{13} \end{pmatrix}, \tag{1.19}$$

where $c_{ij} \equiv \cos\theta_{ij}$ and $s_{ij} \equiv \sin\theta_{ij}$ where i, j are family labels. By convention the mixing angles are taken in the first quadrant, such that $s_{ij}, c_{ij} \geq 0$. The current experimental values are:

$$\begin{aligned} &\sin\theta_{12} = 0.22500 \pm 0.00067, \qquad \sin\theta_{13} = 0.00369 \pm 0.00011, \\ &\sin\theta_{23} = 0.04182^{+0.00085}_{-0.00074}, \qquad \delta = 1.144 \pm 0.027. \end{aligned} \tag{1.20}$$

Since all mixing angles are small, the CKM matrix is approximately diagonal. In particular, the dominant contribution to flavour mixing arises from θ_{12} (the Cabibbo angle), whereas the effects of θ_{23} and θ_{13} are comparatively suppressed. Defining the following four parameters:

$$\lambda \equiv \sin\theta_{12}, \qquad A \equiv \frac{s_{23}}{s_{12}^2}, \qquad \rho \equiv \frac{\mathrm{Re}(s_{13}e^{-i\delta})}{s_{12}s_{23}}, \qquad \eta \equiv -\frac{\mathrm{Im}(s_{13}e^{-i\delta})}{s_{12}s_{23}}, \tag{1.21}$$

the CKM matrix can be conveniently written in the Wolfenstein parametrization as:

$$V = \begin{pmatrix} 1 - \frac{1}{2}\lambda^2 & \lambda & A\lambda^3(\rho - i\eta) \\ -\lambda & 1 - \frac{1}{2}\lambda^2 & A\lambda^2 \\ A\lambda^3(1 - \rho - i\eta) & -A\lambda^2 & 1 \end{pmatrix} + O(\lambda^4), \tag{1.22}$$

The CKM matrix has four independent parameters: three angles and one phase. In the standard parametrisation:

$$V = \begin{pmatrix} c_{12}c_{13} & s_{12}c_{13} & s_{13}e^{-i\delta} \\ -s_{12}c_{23} - c_{12}s_{23}s_{13}e^{i\delta} & c_{12}c_{23} - s_{12}s_{23}s_{13}e^{i\delta} & s_{23}c_{13} \\ s_{12}s_{23} - c_{12}c_{23}s_{13}e^{i\delta} & -c_{12}s_{23} - s_{12}c_{23}s_{13}e^{i\delta} & c_{23}c_{13} \end{pmatrix}, \tag{1.23}$$

with $c_{ij} = \cos\theta_{ij}$, $s_{ij} = \sin\theta_{ij}$. Experimentally, $s_{12} \approx 0.22$, $s_{23} \approx 0.041$, $s_{13} \approx 0.0037$ and $\delta \approx 1.14$ rad. Because of this hierarchy, the Wolfenstein parametrisation is convenient:

$$V_{\mathrm{CKM}} \approx \begin{pmatrix} 1 - \lambda^2/2 & \lambda & A\lambda^3(\rho - i\eta) \\ -\lambda & 1 - \lambda^2/2 & A\lambda^2 \\ A\lambda^3(1 - \rho - i\eta) & -A\lambda^2 & 1 \end{pmatrix} + O(\lambda^4), \tag{1.24}$$

where $\lambda = s_{12} \approx 0.22$, $A \approx 0.84$, and $\bar{\rho} = \rho(1 - \lambda^2/2)$, $\bar{\eta} = \eta(1 - \lambda^2/2)$ are real parameters. The complex phase associated with the non-zero value of $\bar{\eta}$ provides the sole irreducible origin of CP violation within the Standard Model. The unitarity of V implies a set of orthogonality

relations, including

$$V_{ud}V_{ub}^* + V_{cd}V_{cb}^* + V_{td}V_{tb}^* = 0. \tag{1.25}$$

Normalizing the relation by $V_{cd}V_{cb}^*$ gives the unitarity triangle in the complex plane (Fig. 1.2), whose angles are defined by:

$$\alpha = \arg\left(-\frac{V_{td}V_{tb}^*}{V_{ud}V_{ub}^*}\right), \quad \beta = \arg\left(-\frac{V_{cd}V_{cb}^*}{V_{td}V_{tb}^*}\right), \quad \gamma = \arg\left(-\frac{V_{ud}V_{ub}^*}{V_{cd}V_{cb}^*}\right). \tag{1.26}$$

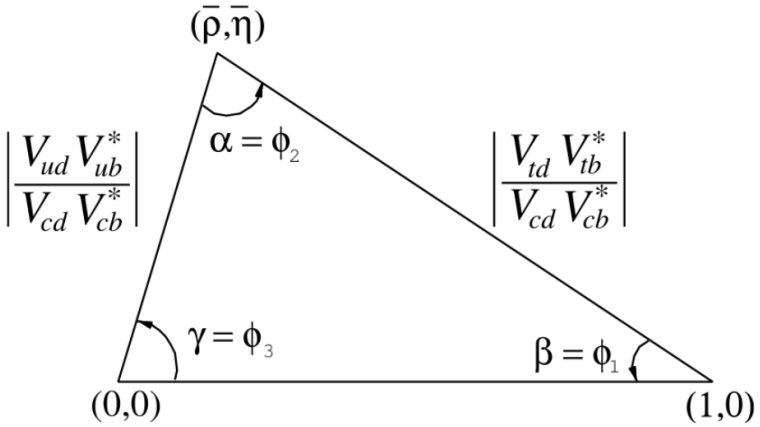

Figure 1.2: Unitarity triangle for $V_{ud}V_{ub}^* + V_{cd}V_{cb}^* + V_{td}V_{tb}^* = 0$.

Precise determinations of the unitarity-triangle angles (especially β and γ) are among the central goals of the LHCb physics programme.

1.4 CP Violation in mesons systems

In addition to precision measurements of the CKM unitarity triangle in the beauty sector, studies of CP violation in the charm sector provide a complementary probe of flavour physics. For a generic meson P and its CP conjugate $\bar{P}$, we define the decay amplitudes[6] to a final state f (and its CP-conjugate $\bar{f}$) as:

$$\begin{aligned} A_f &= \langle f|\mathcal{H}|P\rangle, & \bar{A}_{\bar{f}} &= \langle \bar{f}|\mathcal{H}|\bar{P}\rangle, \\ \bar{A}_f &= \langle f|\mathcal{H}|\bar{P}\rangle, & A_{\bar{f}} &= \langle \bar{f}|\mathcal{H}|P\rangle, \end{aligned} \tag{1.27}$$

where $\mathcal{H}$ is the weak interaction Hamiltonian[7]. Under a CP transformation, the amplitudes transform as $A_f \leftrightarrow \bar{A}_{\bar{f}}$, up to possible phase conventions. The complex phases of the CKM

[6]The amplitude A_f is the quantum mechanical transition matrix element between these states.
[7]The effective weak Hamiltonian describing the weak decay at low energies.

matrix elements introduce a weak phase ϕ_i, which changes sign under CP conjugation. In addition, absorptive contributions from on-shell intermediate states generate a strong phase δ_i, which is CP-invariant. The decay amplitudes can therefore be written as:

$$A_f = \sum_i |A_i| e^{i(\delta_i + \phi_i)}, \qquad \bar{A}_{\bar{f}} = \sum_i |A_i| e^{i(\delta_i - \phi_i)}. \tag{1.28}$$

For charged mesons, CP violation can only manifest as direct CP asymmetry in decay rates:

$$A_{CP} = \frac{\Gamma(P \to f) - \Gamma(\bar{P} \to \bar{f})}{\Gamma(P \to f) + \Gamma(\bar{P} \to \bar{f})} = \frac{|A_f|^2 - |\bar{A}_{\bar{f}}|^2}{|A_f|^2 + |\bar{A}_{\bar{f}}|^2}. \tag{1.29}$$

CP violation occurs when $|A_f / \bar{A}_{\bar{f}}| \neq 1$. This requires the interference of at least two decay amplitudes with different weak and strong phases. Neutral mesons (P^0, $\bar{P}^0$) exhibit an additional phenomenon: flavour oscillations induced by second-order weak interactions allow them to mix with their antiparticles. This mixing gives rise to two mass eigenstates:

$$|P_1\rangle = p|P^0\rangle + q|\bar{P}^0\rangle, \qquad |P_2\rangle = p|P^0\rangle - q|\bar{P}^0\rangle, \tag{1.30}$$

with $|p|^2 + |q|^2 = 1$. The complex parameter q/p characterises flavour mixing in the neutral meson system. The time evolution of an initial state $|P^0\rangle$ or $|\bar{P}^0\rangle$ exhibits oscillatory behaviour, leading to interference between decay amplitudes with and without mixing. The physical mass eigenstates are defined as

$$|P_{H,L}\rangle = p|P^0\rangle \pm q|\bar{P}^0\rangle, \tag{1.31}$$

where the subscripts H and L denote the heavy and light eigenstates, respectively. Their masses and decay widths are given by $M_{H,L}$ and $\Gamma_{H,L}$, with average width $\Gamma = (\Gamma_H + \Gamma_L)/2$. It is then convenient to introduce the dimensionless mixing parameters

$$x = \frac{M_H - M_L}{\Gamma}, \qquad y = \frac{\Gamma_H - \Gamma_L}{2\Gamma}. \tag{1.32}$$

These parameters quantify the strength of flavour oscillations in the neutral meson system. In neutral mesons, three distinct types of CP violation can be identified: direct CP violation ($|\bar{A}_f / A_f| \neq 1$); CP violation in mixing ($|q/p| \neq 1$), implying that the mass eigenstates are not CP eigenstates; and CP violation in the interference between mixing and decay ($\mathrm{Im}((q/p) \cdot (\bar{A}_f / A_f)) \neq 0$ for a CP eigenstate f), which can occur even if the previous two conditions are satisfied.

1.4.1 Detection asymmetry for $K\pi$ pairs

The discussion above concerns the different sources of CP violation that can arise in neutral meson systems. However, in an experimental environment such as a hadron collider, these effects are not directly observable. Instead, what is measured is a so-called raw asymmetry, which generally differs from the underlying physical CP asymmetry due to additional contributions from production and detection effects:

$$A_{\text{raw}} \approx A_{CP} + A_{\text{prod}} + A_{\text{det}}. \tag{1.33}$$

A_{prod} is the production asymmetry arising an imbalance in the initial quark content in pp collisions, defined as:

$$A_{\text{prod}} = \frac{\sigma(D^+) - \sigma(D^-)}{\sigma(D^+) + \sigma(D^-)} \tag{1.34}$$

The asymmetry is generated because a D^+ meson shares valence quarks with the proton more frequently than a D^-. The detection asymmetry is defined as:

$$A_{\text{det}}(K^-\pi^+) = \frac{\varepsilon(K^-\pi^+) - \varepsilon(K^+\pi^-)}{\varepsilon(K^-\pi^+) + \varepsilon(K^+\pi^-)} \tag{1.35}$$

where ε denotes the reconstruction efficiency. To isolate A_{det}, control channels with known negligible A_{CP} are used: the decays $D^+ \to K^-\pi^+\pi^+$ (denoted $K\pi\pi$) and $D^+ \to K^0_S\pi^+$ (denoted $K_S\pi$), together with their charge conjugates. These are Cabibbo-favoured decays, for which the Standard Model predicts $A_{CP} \sim 10^{-4}$ or smaller, making them suitable control modes. Writing the raw asymmetries for the two channels [12]:

$$\begin{aligned} A_{\text{raw}}(K\pi\pi) &\approx A_{CP}(K\pi\pi) + A_{\text{prod}}(D^+) + A_{\text{det}}(K^-\pi^+) + A_{\text{det}}(\pi^+), \\ A_{\text{raw}}(K_S\pi) &\approx A_{CP}(K_S\pi) + A_{\text{prod}}(D^+) + A_{\text{det}}(K^0_S) + A_{\text{det}}(\pi^+). \end{aligned} \tag{1.36}$$

Since both decay modes originate from the same initial D^+ meson, several common contributions cancel in the difference of the raw asymmetries. In particular, the production asymmetry $A_{\text{prod}}(D^+)$ cancels exactly, as well as the detection asymmetry associated with the bachelor pion $A_{\text{det}}(\pi^+)$. Moreover, the CP asymmetries of both channels are expected to be negligible within the Standard Model. This leads to a direct relation between the difference of the raw asymmetries:

$$A_{\text{raw}}(K\pi\pi) - A_{\text{raw}}(K_S\pi) = A_{\text{det}}(K^-\pi^+) - A_{\text{det}}(K^0_S). \tag{1.37}$$

This relation allows one to extract the kaon–pion detection asymmetry once the neutral-kaon contribution is known from independent measurements. Using external input for $A_{\text{det}}(K^0_S)$, the detection asymmetry $A_{\text{det}}(K^-\pi^+)$ can be determined as:

$$A_{\text{det}}(K^-\pi^+) = A_{\text{raw}}(K\pi\pi) - A_{\text{raw}}(K_S\pi) + A_{\text{det}}(K^0_S). \tag{1.38}$$

Chapter 2

The LHCb experiment

The Large Hadron Collider (LHC) is the world's largest particle [14]. It is installed in a 27 km underground tunnel and is located about 100 m below the border between France and Switzerland, near Geneva. The LHC is designed to collide proton beams and, during the Run 3 data-taking campaign (2022-2026), it has operated at a centre-of-mass energy of $\sqrt{s} = 13.6$ TeV with a peak luminosity of $\mathcal{L} = 2 \times 10^{33}$ cm^{-2}s^{-1}. The LHC is composed of 1232 superconducting dipole magnets that provide a magnetic field of 8.33 T, cooled at 1.9 K by superfluid helium [15]. These magnets bend the proton beams along the circular trajectory. Additionally, 392 quadrupole magnets and other multipoles help focus and correct the beam trajectory. Before injection into the LHC, protons are pre-accelerated in a chain of increasingly powerful machines (Figure 2.1). Protons are extracted from hydrogen atoms and accelerated through the Linac 2, PSB (Proton Synchrotron Booster), and PS, finally reaching 450 GeV in the Super Proton Synchrotron (SPS). From the SPS, the protons are injected into the LHC, where they are ramped up to their final energy (6.8 TeV per beam during Run 3).

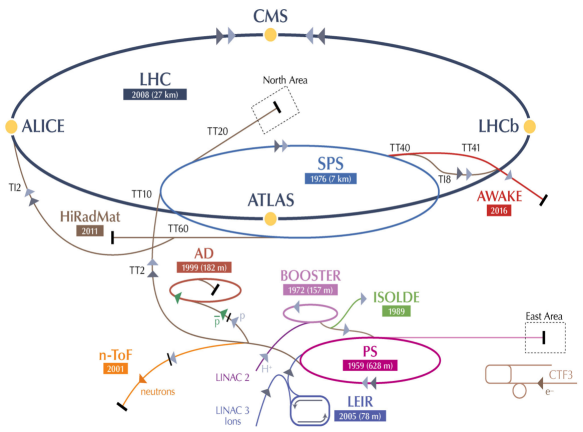

Figure 2.1: The CERN accelerator infrastructure.

The proton beams are organised into bunches containing approximately 10^{11} protons each. At the interaction points, the bunches cross every 25 ns, producing on average about 20 visible

proton–proton collisions per bunch crossing during Run 3 conditions. The LHC hosts four main experiments: ATLAS, CMS, ALICE, and LHCb. The LHCb (Large Hadron Collider beauty) experiment is a single-arm forward spectrometer designed for precision studies of flavour physics, with particular emphasis on CP violation and rare decays of hadrons containing beauty and charm quarks. Its forward geometry is motivated by the production kinematics of heavy quarks at high energies. In proton–proton collisions, $b\bar{b}$ and $c\bar{c}$ quark pairs are predominantly produced at small angles with respect to the beam axis, causing both heavy hadrons to emerge in the same forward or backward region. Approximately 30% of the produced beauty hadrons fall within the LHCb geometrical acceptance, providing large samples of beauty and charm decays while maintaining a relatively compact detector design and manageable readout complexity.

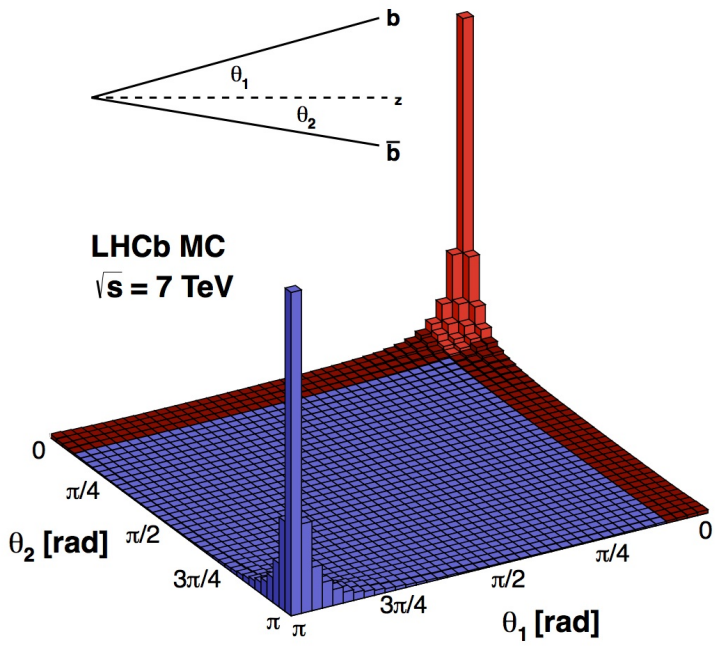

Figure 2.2: Angular distribution of $b\bar{b}$ pairs simulated at $\sqrt{s} = 14$ TeV. The acceptance of the LHCb detector is shown in red. Most pairs are produced in the forward or backward direction, justifying the single-arm forward spectrometer geometry.

2.1 LHCb detector layout

The LHCb detector (Figure 2.3) is composed of several subdetectors arranged sequentially along the beam line. The main components, listed from the interaction point outward, are:

- *Vertex Locator (VELO)*, it surrounds the interaction region and provides precise recon-

struction of primary and secondary vertices;

- *Beam pipe*, a series of conical sections made of beryllium and stainless steel, separating the detector vacuum from the accelerator vacuum;
- *RICH1*, a Ring Imaging Cherenkov detector located upstream of the magnet, dedicated to low-momentum particle identification (PID);
- *Tracking system*, originally composed of the Trigger Tracker (TT) upstream of the magnet and three tracking stations (T1–T3) downstream of it. During the Run 3 upgrade, the TT was replaced by the Upstream Tracker (UT), while the T1–T3 stations were replaced by the Scintillating Fibre Tracker (SciFi).
- *Dipole magnet*, provides a vertical magnetic field that bends charged particles in the horizontal plane, allowing the measurement of their momentum and charge;
- *RICH2*, located downstream of the magnet and optimised for high-momentum particle identification;
- *Calorimeter system*, composed of the Scintillating Pad Detector (SPD), the Pre-Shower detector (PS), the electromagnetic calorimeter (ECAL), and the hadronic calorimeter (HCAL). In the upgraded Run 3 detector, the SPD and PS systems were removed;
- *Muon system*, originally composed of five stations (M1–M5) equipped with multi-wire proportional chambers and triple-GEM detectors for muon identification. In the Run 3 upgraded detector, the M1 station was removed;
- *Trigger and data acquisition system*, a two-level software trigger system (HLT1 and HLT2) that reduces the event rate from the 40 MHz bunch-crossing frequency to approximately 12 kHz for permanent storage.

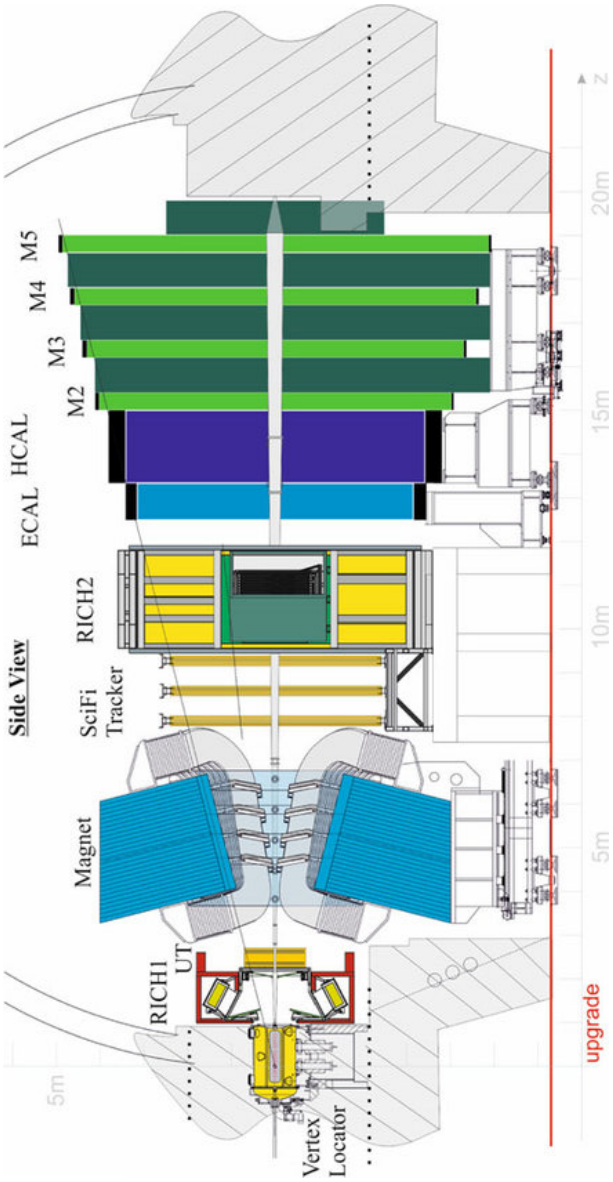

Figure 2.3: View of the LHCb detector.

In the following sections, each subdetector is described in detail with emphasis on the upgrades relevant for Run 3.

2.1.1 The Vertex Locator (VELO)

The Vertex Locator (VELO) is the subdetector closest to the interaction point and is designed to precisely reconstruct primary pp vertices and secondary vertices from beauty and charm decays. Beauty and charm hadrons have lifetimes of the order 10^{-12} s, traveling a few millimetres before decaying. The VELO must therefore provide excellent impact parameter resolution (the distance of closest approach of a track to the primary vertex). The required resolution is about 40 µm in the z direction and 10 µm in the transverse plane. The VELO consists of 52 silicon modules arranged along the beam axis, covering a region from about

5 cm upstream to 80 cm downstream of the interaction point. Each module provides a measurement of the radial distance r from the beam axis (via r-sensors) and the azimuthal angle ϕ (via ϕ-sensors), as shown in Figures 2.4. This r-ϕ geometry allows fast track reconstruction and vertexing. The sensors are made of n-on-p silicon, with a thickness of 200 µm and a pixel pitch of 55×55 μm^2 in the upgraded VELO (Run 3). The VELO modules are mounted on two movable halves that can be retracted to 3 cm from the beam during beam injection and acceleration, and closed to 5.1 mm during stable operation. A 250 µm thick aluminium RF foil separates the detector vacuum from the beam vacuum, minimising material before the sensors while protecting the sensors from RF pickup.

Simulations show that the upgraded VELO achieves $\varepsilon_{\text{rec}} > 98.9\%$ for most tracks, and up to 99.8% for tracks with high transverse momentum[16].

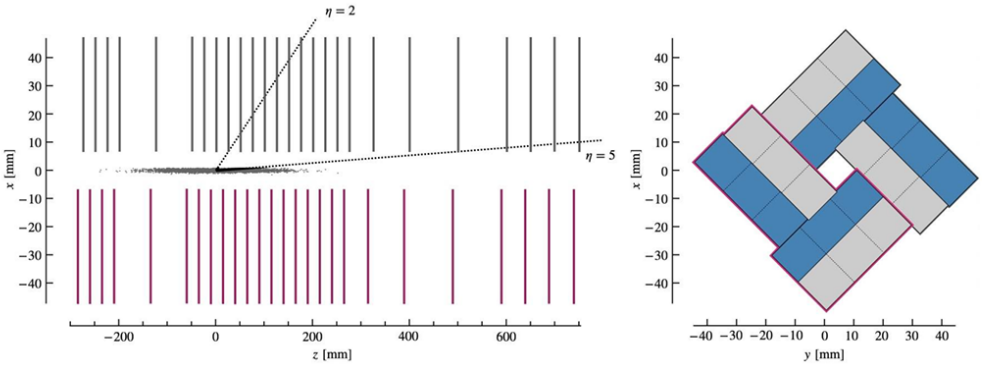

Figure 2.4: VELO detector layout. The longitudinal profile (x-z plane) is displayed on the left, while the transverse cross-section (x-y plane) is presented on the right. Side C is distinguished by purple highlighting.

2.1.2 Upstream tracker (UT) and Scintillating Fibres (SciFi) tracker

The tracking system of LHCb measures the trajectories of charged particles after they exit the VELO and traverse the magnet.

The Upstream Tracker is a silicon strip tracking sub-detector, placed between the RICH1 detector and the dipole magnet. It is used for charged-particle tracking and it is an essential component for the first processing algorithm in the software trigger. Indeed, the UT hits in combination with the VELO tracks allow a first determination of the track momentum p with moderate precision (approximately 15%). Moreover, tracks with $p_T > 0.2$ GeV are processed and an estimate of momentum and charge is performed to speed up the matching with the SciFi Tracker results. UT hit information also reduces the rate of fake tracks due to VELO and SciFi segments and provides measurements for long lived particles, that decay after the VELO. The SciFi tracker is the last part of the detector which aims at particle tracking and momentum measurements. This tracker is expected to provide a hit position resolution better than 100 μm in the magnet bending plane and single hit reconstruction efficiency better than

99%, good radiation hardness (able to maintain the desired performance over the complete lifetime of the experiment, which aims at collecting 50 fb^1 of integrated luminosity), while also having low material budget to limit multiple scattering and low occupancy. A schematic of the SciFi tracker is shown in Fig. 2.5

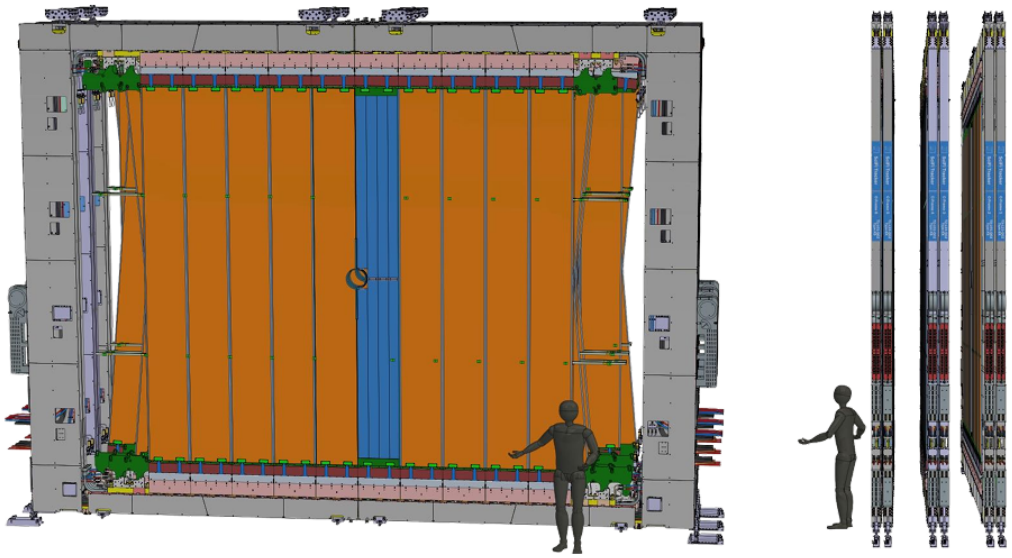

Figure 2.5: Schematic of the SciFi sub-detector. The transverse projection (x-y plane) is shown on the left, while the longitudinal projection (y-z plane) is on the right. In the transverse view, the scintillating fibre mats are highlighted in blue, and an individual layer module is demarcated in orange.

2.1.3 The Dipole Magnet

The LHCb dipole magnet is a warm (non-superconducting) magnet with saddle-shaped coils mounted in a window-frame yoke. It is approximately 3.6 m high, 5 m long, and each coil has a mass of about 27 tonnes. The magnet provides a magnetic field predominantly in the vertical (y) direction, with an integrated field of about 4 Tm over the magnet region.

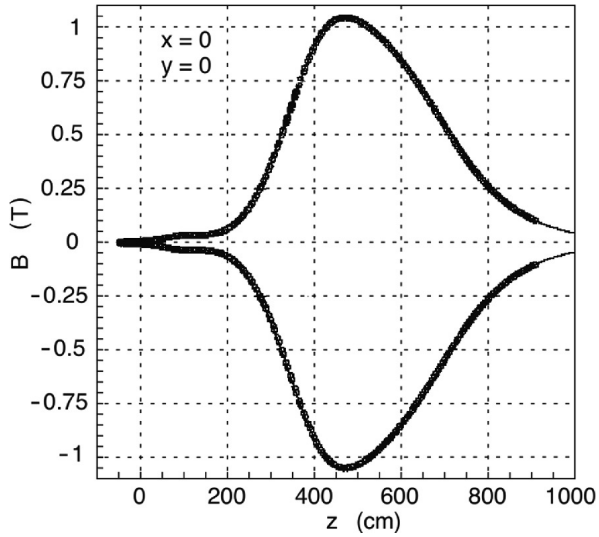

Figure 2.6: Magnetic field along the direction of the beam (z) within the LHCb detector [15].

Charged particles traversing the magnet are bent in the horizontal (x–z) plane, and the curvature of their trajectories is used to determine their momentum. The momentum resolution is of order $\delta p/p \approx 0.5$–1%, depending on the momentum and detector acceptance. To control systematic effects, the magnet polarity is reversed every few weeks. Data taken with the field pointing upward (positive y direction) are referred to as *MagUp*, while data taken with the opposite polarity are referred to as *MagDown*. This periodic reversal is essential in CP violation measurements, as it helps cancel detector-induced asymmetries that depend on the bending direction, such as left–right differences in tracking efficiency. In this thesis, data from both polarities are analysed separately and then combined.

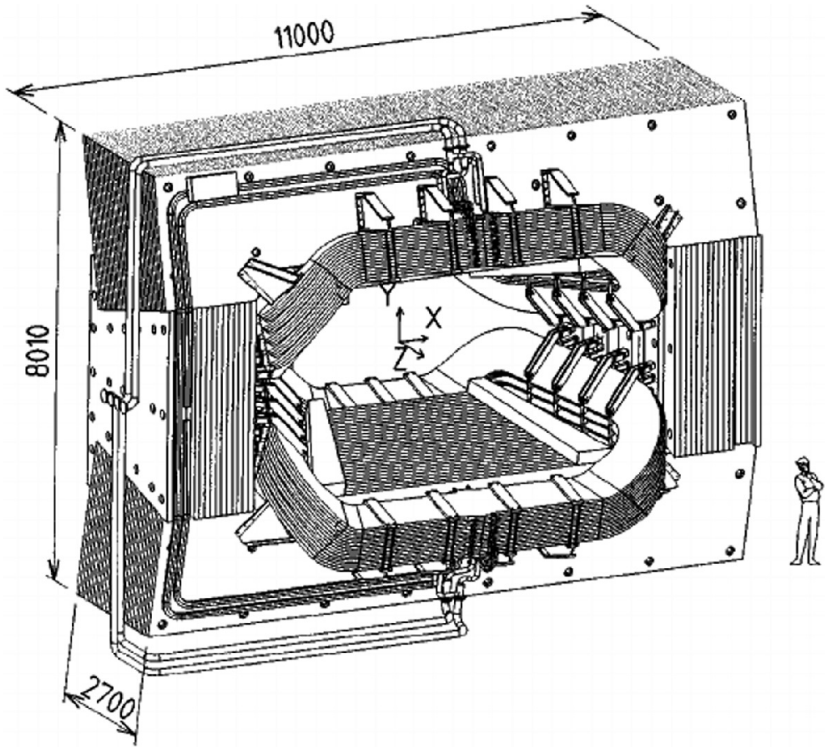

Figure 2.7: Sketch of the dipole magnet in the LHCb detector [15].

2.2 Particle identification systems

Particle identification (PID) is fundamental for LHCb, especially for separating kaons from pions, which is critical for CP violation measurements in $D^0 \to K^-K^+$ and $D^0 \to \pi^-\pi^+$ decays. The LHCb PID system relies mainly on two Ring Imaging Cherenkov (RICH) detectors, supplemented by the calorimeters and muon system.

2.2.1 Principle of Cherenkov detection

When a charged particle traverses a transparent medium (radiator) with a velocity exceeding the phase velocity of light in that medium, it emits Cherenkov radiation. The Cherenkov angle θ_C is given by

$$\cos\theta_C = \frac{1}{n\beta}, \tag{2.1}$$

where n is the refractive index of the radiator and $\beta = v/c$.

For a particle of known momentum $p = \gamma mv$, the Cherenkov angle provides information on its mass, and therefore allows particle identification. By measuring both the momentum (from tracking) and the Cherenkov angle, the particle species can be identified. The emitted photons form a cone that is reflected by spherical and flat mirrors and focused onto photon detectors, where they are detected as a ring-like pattern.

2.2.2 RICH1 and RICH2

RICH1, schematically shown in Fig. 2.8, is located between the VELO and the magnet (originally between the VELO and the TT station). It covers the forward angular acceptance of the LHCb detector, corresponding approximately to polar angles of 25–300 mrad in the horizontal plane and 25–250 mrad in the vertical plane. It employs a gaseous radiator, textitC_4F_{10} gas (refractive index $n \approx 1.0014$), providing particle identification in the momentum range between approximately 2.5 and 6 0 GeV/c.

The radiator choice for RICH1 ensures efficient particle identification over a wide momentum range. The Cherenkov photons are reflected by a spherical mirror and a system of flat mirrors, which focus the light outside the detector acceptance, where it is detected by multi-anode photomultiplier tubes (MaPMTs) with improved timing resolution and higher readout speed.

RICH2, schematically shown in Fig. 2.9, is located downstream of the magnet, between the SciFi tracker and the calorimeter system. It has a narrower angular acceptance, covering approximately 15–120 mrad in the horizontal plane and 15–100 mrad in the vertical plane. It employs a single gaseous radiator, CF_4 (refractive index $n \approx 1.0005$), which is optimised for high-momentum particle identification, typically for particles with momenta above approximately 15 GeV/c up to about 100 GeV/c. The optical system is similar to that of RICH1, with spherical and flat mirrors used to focus the Cherenkov photons onto photon detectors located outside the acceptance region.

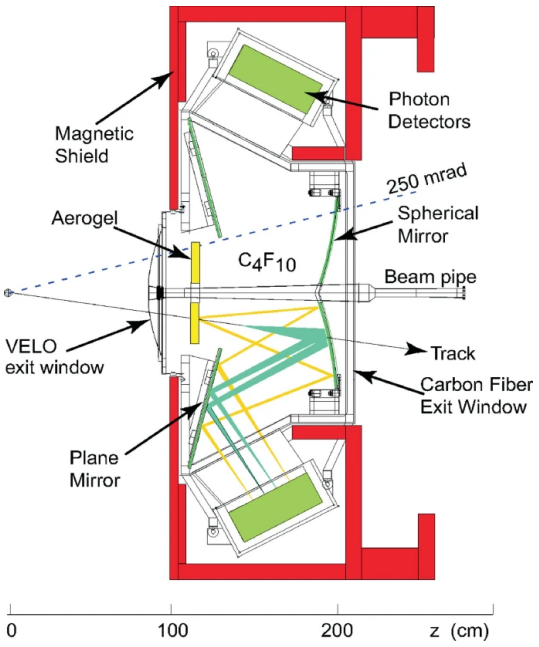

Figure 2.8: Layout of the RICH1 detector.

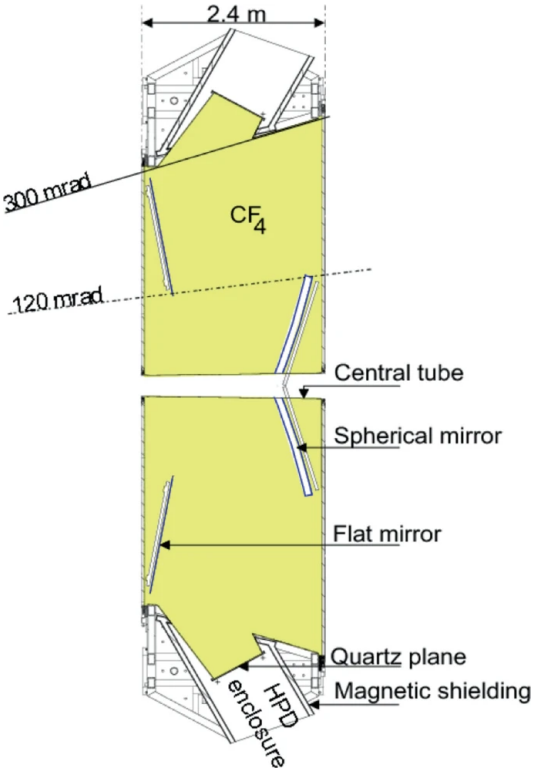

Figure 2.9: Layout of the RICH2 detector.

2.3 Calorimeter System

The calorimeter system consists of the following subdetectors (from upstream to downstream):

- *Electromagnetic Calorimeter (ECAL)*, a shashlik sampling calorimeter composed of alternating lead (2 mm) and scintillator (4 mm) layers, corresponding to a total depth of approximately 25 radiation lengths. The energy resolution is $\sigma_E/E = 9\%/\sqrt{E} \oplus 0.8\%$ (with E in GeV). The calorimeter is segmented into inner, middle, and outer regions with cell sizes of 4×4, 6×6, and $12 \times 12\,\mathrm{cm}^2$, respectively;

- *Hadronic Calorimeter (HCAL)*, a sampling calorimeter using iron absorber plates (16 mm) interleaved with plastic scintillator layers (4 mm), corresponding to a total depth of about 5.6 interaction lengths. The energy resolution is $\sigma_E/E = 67.5\%/\sqrt{E} \oplus 9\%$. It is segmented into inner and outer regions with cell sizes of $13 \times 13\,\mathrm{cm}^2$ and $26 \times 26\,\mathrm{cm}^2$, respectively.

The elementary detection cells for ECAL and HCAL are shown in Fig. 2.10

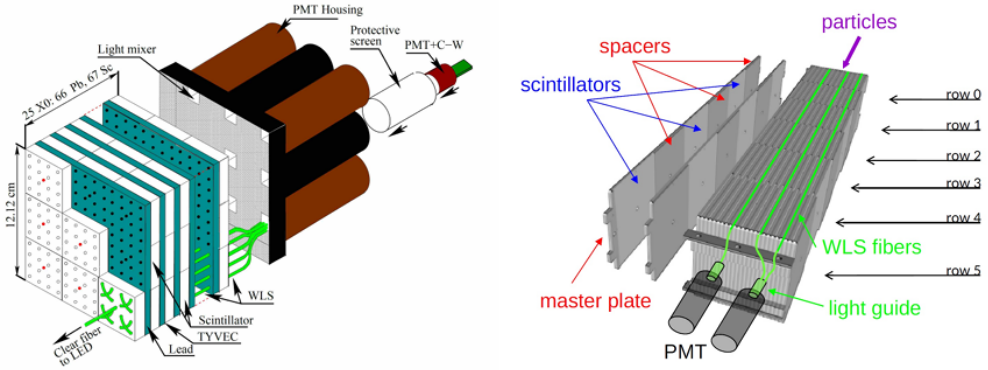

(a) ECAL cell (b) HCAL cell

Figure 2.10: ECAL (left) and HCAL (right) unit cell schematics.

2.4 Muon System

The muon system provides identification of muons and plays a crucial role in the LHCb trigger, rather than measuring particle momentum, which is determined by the tracking system. It consists of four stations (M2–M5). Station M1 was removed before the start of Run 3. Stations M2–M5 are placed downstream of the hadronic calorimeter (HCAL), interleaved with 80 cm thick iron absorbers that suppress hadrons. Only muons are typically able to traverse the absorber material and reach the downstream stations. The muon system covers the same angular acceptance as the rest of the LHCb detector. Each station is divided into four regions (R1–R4), with increasing cell size towards larger radii to accommodate decreasing particle flux away from the beam pipe. Multi-wire proportional chambers (MWPCs) are used in regions R2–R4 of all statios. A schematic view of the muon system is shown in Fig. 2.11.

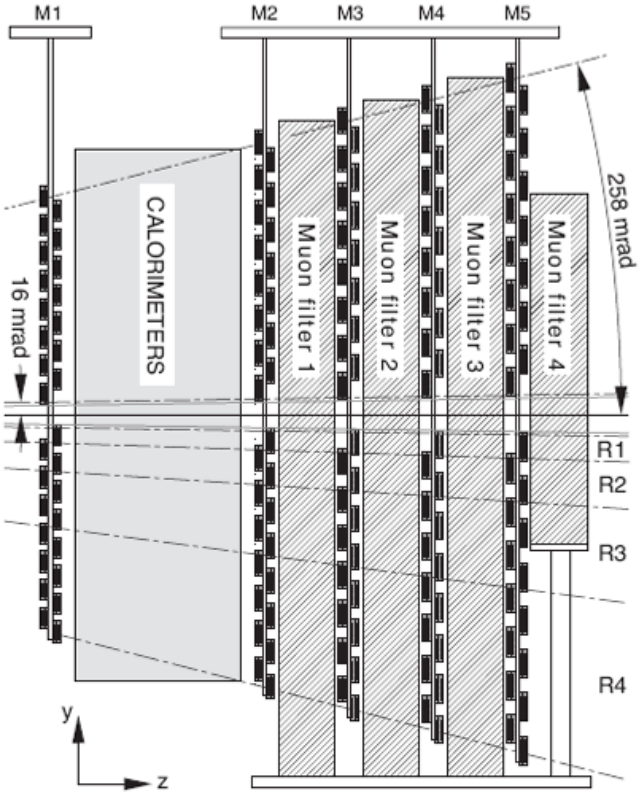

Figure 2.11: Muon system (y-z plane).

2.5 Trigger and Data Acquisition System

The LHC produces proton–proton collision events at a rate of 40 MHz, but only a small fraction can be stored for offline analysis. In the upgraded LHCb detector (Run 3), the traditional hardware-based Level-0 (L0) trigger has been removed and replaced by a fully software-based, trigger-less readout architecture. As a consequence, all events are transferred directly to the software trigger farm without an initial hardware selection. Nevertheless, the two-stage structure is preserved. *High Level Trigger 1 (HLT1)* performs a fast partial reconstruction, including basic tracking and primary vertex reconstruction, and reduces the event rate to a manageable level. *High Level Trigger 2 (HLT2)* then performs a full offline-quality reconstruction and applies a wide range of selection algorithms ("trigger lines") tailored to specific physics channels [14].

2.6 Detector Induced Asymmetries

Detector-induced asymmetries represent an important limitation in precision measurements of CP and production asymmetries at LHCb. Despite the excellent performance of the detector,

small charge-dependent effects arise due to the interaction of particles with the detector material and differences in reconstruction efficiencies. In particular, hadronic interaction cross-sections for charged kaons are not identical for positive and negative charges, leading to momentum-dependent efficiency differences. Similar effects arise for charged pions due to small asymmetries in tracking and reconstruction performance. These effects motivate the use of control channels with negligible intrinsic CP asymmetry, which allow detector-induced contributions to be constrained experimentally, as discussed in Chapter 1.

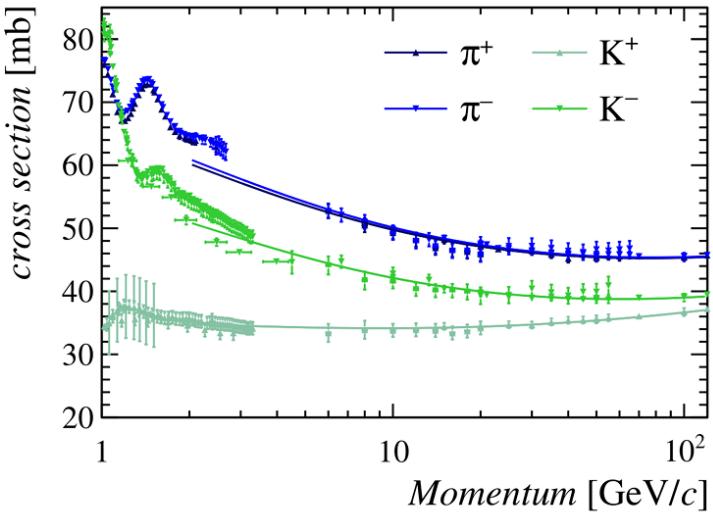

Figure 2.12: Momentum dependence of $\pi^{\pm}$ and $K^{\pm}$ total cross-sections on deuterium. The data highlights a clear charge asymmetry in the kaon sector at lower momentum scales.

The extraction method is the subject of the next chapter. In Run 2, the LHCb collaboration measured $A_{\text{det}}(K^-\pi^+) = (-0.89 \pm 0.15 \pm 0.06)\%$ (2015) and $(-1.03 \pm 0.06 \pm 0.06)\%$ (2016).

Chapter 3

Measurement of the $K^-\pi^+$ detection asymmetry

This chapter describes the experimental extraction of the detection asymmetry $A_{\text{det}}(K^-\pi^+)$ using part of the Run 3 data collected by the LHCb experiment. The analysis strategy follows the formalism developed in Chapter 1.

3.1 Motivation and observable definition

A fundamental input for the measurement of CP asymmetries in charmed hadron decays is the detection asymmetry of the $K^-\pi^+$ pair, named $A_{\text{det}}(K^-\pi^+)$. Unlike production asymmetries, detection asymmetries originate from the experimental apparatus. Differences in the interaction cross-sections of K^+ and K^- with the LHCb detector material, as well as differences in track reconstruction efficiencies, introduce a bias in the observed number of particles and anti-particles.

As discussed in Chapter 1, this detection asymmetry can be measured using the decay modes $D^+ \to K^-\pi^+\pi^+$ and $D^+ \to K_S\pi^+$, exploiting the cancellation of common terms described in Eq. (1.33).

3.2 Choice of control channels

The decay channels chosen to extract the detection asymmetry of the $K\pi$ pair are:

- $D^+ \to K^-\pi^+\pi^+$ (hereafter referred to as $K\pi\pi$),
- $D^+ \to K_S\pi^+$ with $K_S \to \pi^+\pi^-$ (hereafter referred to as $K_S\pi$),

together with their charge-conjugate modes. These decays are Cabibbo-favoured, with CP-violating asymmetries expected to be well below 10^{-4}, making them ideal for this purpose.

The choice of these two specific channels is motivated by several considerations. The $K\pi\pi$ decay mode is particularly advantageous since it contains the same $K^-\pi^+$ pair, while the additional π^+ allows the cancellation of the pion detection asymmetry $A_{\text{det}}(\pi^+)$ in the subtraction procedure. The $K_S\pi$ decay mode, on the other hand, provides a $K_S \to \pi^+\pi^-$ pair, whose detection asymmetry is known to be very small and the CP violation in the neutral kaon system is negligible. The bachelor pion present in both decays ensures that $A_{\text{det}}(\pi^+)$ appears identically in the raw asymmetry expressions for both channels.

The raw asymmetries for the two channels are defined as:

$$A_{\text{raw}}(K\pi\pi) = \frac{N(D^+ \to K^-\pi^+\pi^+) - N(D^- \to K^+\pi^-\pi^-)}{N(D^+ \to K^-\pi^+\pi^+) + N(D^- \to K^+\pi^-\pi^-)}, \tag{3.1}$$

$$A_{\text{raw}}(K_S\pi) = \frac{N(D^+ \to K_S\pi^+) - N(D^- \to K_S\pi^-)}{N(D^+ \to K_S\pi^+) + N(D^- \to K_S\pi^-)}. \tag{3.2}$$

3.3 Decomposition of the raw asymmetry

The raw asymmetry for a charged D meson decay can be decomposed into several contributions. To first order, as introduced in Eq. (1.30), it can be approximated as the sum of three distinct components: the CP asymmetry A_{CP}, the production asymmetry A_{prod}, and the detection asymmetry A_{det}.

$$A_{\text{raw}}(K\pi\pi) \approx A_{CP}(K\pi\pi) + A_{\text{prod}}(D^+) + A_{\text{det}}(K^-\pi^+) + A_{\text{det}}(\pi^+), \tag{3.3}$$

$$A_{\text{raw}}(K_S\pi) \approx A_{CP}(K_S\pi) + A_{\text{prod}}(D^+) + A_{\text{det}}(K_S) + A_{\text{det}}(\pi^+). \tag{3.4}$$

Since both decay modes are Cabibbo-favoured, their intrinsic CP asymmetries are negligible ($A_{CP} \approx 0$). The production asymmetry $A_{\text{prod}}(D^+)$ and the pion detection asymmetry $A_{\text{det}}(\pi^+)$ are common to both channels. Subtracting Eq. (3.4) from Eq. (3.3) therefore cancels these common terms:

$$A_{\text{raw}}(K\pi\pi) - A_{\text{raw}}(K_S\pi) = A_{\text{det}}(K^-\pi^+) - A_{\text{det}}(K_S). \tag{3.5}$$

The term $A_{\text{det}}(K_S)$ accounts for the detection asymmetry of the K_S meson, which is non-zero due to the admixture of K_L and K_S components in the neutral kaon decay. Its value is known from external measurements and, once inserted, allows the detection asymmetry for the $K\pi$ pair to be expressed as:

$$A_{\text{det}}(K^-\pi^+) = A_{\text{raw}}(K\pi\pi) - A_{\text{raw}}(K_S\pi) + A_{\text{det}}(K_S). \tag{3.6}$$

The raw asymmetries entering this relation are obtained from fits to the invariant-mass distributions of the relevant decays, as described in the following sections. The results obtained by analyzing the data from the two polarities are averaged to cancel instrumental asymmetries:

$$A^{\mathrm{avg}}(K\pi\pi) = \frac{A^{\mathrm{Up}}(K\pi\pi) + A^{\mathrm{Down}}(K\pi\pi)}{2}, \tag{3.7}$$

$$A^{\mathrm{avg}}(K_S\pi) = \frac{A^{\mathrm{Up}}(K_S\pi) + A^{\mathrm{Down}}(K_S\pi)}{2}. \tag{3.8}$$

The statistical uncertainties are propagated accordingly. The final detection asymmetry is then computed using the averaged raw asymmetries, and the total uncertainty includes the contribution from $A_{\mathrm{det}}(K_S)$.

3.4 Experimental procedure overview

The extraction of $A_{\mathrm{det}}(K^-\pi^+)$ proceeds through several steps, which are described in detail in the following sections. A schematic overview is provided here for clarity.

Step 1: Sample selection. The analysis uses part of the 2024 LHCb Run 3 data and the two decay channels $D^+ \to K^-\pi^+\pi^+$ and $D^+ \to K_S\pi^+$. Only events passing the baseline quality requirements are retained. The baseline requirements include cuts on the transverse momentum of the particles, their impact parameter with respect to the primary pp interaction vertices, as well as criteria on the particle identification variables provided by the RICH detectors [19].

Step 2: Maximum likelihood fit. For each decay channel and each magnet polarity (Up and Down), a maximum likelihood fit is performed to the invariant mass distribution of $D^\pm$ candidates. The signal is modelled using a Johnson S_U function supplemented by two Gaussian components, all sharing a common mean corresponding to the $D^\pm$ mass. The combinatorial background is described by an exponential function. The fit is performed simultaneously for D^+ and D^- candidates, allowing the raw asymmetry A_{raw} to be extracted directly as a fit parameter.

Step 3: Magnet averaging. To cancel instrumental asymmetries that may depend on the polarity of the LHCb magnet, the raw asymmetries obtained from the data corresponding to Up and Down magnet polarities are averaged for each decay channel, as already defined in Eqs. (3.7) and (3.8).

Step 4: Detection asymmetry extraction. Using the averaged raw asymmetries, the detection asymmetry for the $K^-\pi^+$ pair is computed as:

$$A_{\text{det}}(K^-\pi^+) = A^{\text{avg}}(K\pi\pi) - A^{\text{avg}}(K_S\pi) + A_{\text{det}}(K_S), \tag{3.9}$$

where $A_{\text{det}}(K_S)$ is the detection asymmetry of the neutral kaon.

3.5 Fit model

The raw asymmetries are extracted from a simultaneous fit to the invariant-mass distributions of D^+ and D^- candidates. For each decay channel ($K\pi\pi$ and $K_S\pi$) and each magnet polarity (Up and Down), a binned maximum-likelihood fit is performed over the mass range 1800–1950 MeV/c^2 (1800–1930 MeV/c^2 for the $K_S\pi$ channel). The fit is performed on histogrammed data with 200 bins in the mass range, a choice that balances statistical stability and resolution.

The probability density function (PDF) for D^+ and D^- mesons is:

$$P_\pm(m) = \frac{N^\pm_{\text{sig}}}{N^\pm_{\text{sig}} + N^\pm_{\text{bkg}}}\, S(m) + \frac{N^\pm_{\text{bkg}}}{N^\pm_{\text{sig}} + N^\pm_{\text{bkg}}}\, B(m), \tag{3.10}$$

with the yields parameterised as

$$N^\pm_{\text{sig}} = \frac{N^{\text{tot}}_{\text{sig}}}{2}\,(1 \pm A^{\text{sig}}_{\text{raw}}), \qquad N^\pm_{\text{bkg}} = \frac{N^{\text{tot}}_{\text{bkg}}}{2}\,(1 \pm A^{\text{bkg}}_{\text{raw}}). \tag{3.11}$$

Signal model. The signal shape $S(m)$ is modelled by the sum of a Johnson S_U distribution and two Gaussian functions, all sharing a common mean μ (the $D^\pm$ mass). The Johnson S_U distribution is

$$J(m;\mu,\sigma,\gamma,\delta) = \frac{\delta}{\sigma\sqrt{2\pi(1+z^2)}} \exp\left[-\frac{1}{2}\left(\gamma + \delta \sinh^{-1} z\right)^2\right], \qquad z = \frac{m-\mu}{\sigma}, \tag{3.12}$$

where μ, σ are location and scale, γ, δ control asymmetry and kurtosis. The complete signal PDF is

$$S(m) = f_1\, J(m;\mu,\sigma,\gamma,\delta) + (1-f_1)\left[f_2\, G(m;\mu,\sigma_1) + (1-f_2)\, G(m;\mu,\sigma_2)\right], \tag{3.13}$$

with $G(m;\mu,\sigma_i)$ ordinary Gaussians of the same mean μ and widths σ_1, σ_2, and f_1, f_2 fraction parameters.

Background model. The combinatorial background is described by an exponential function:

$$B(m) = e^{\tau m}. \tag{3.14}$$

The exponential parameter τ has been initialized to $-0.001\,\mathrm{MeV}^{-1}c^2$, with an allowed range of $[-0.01, 0]$. Over the narrow mass window (about 150 MeV/c^2) the exponential is approximately linear, providing a flexible description.

Fit implementation. The fit is performed using the RooFit package. A simultaneous PDF combines the two charge categories. All shape parameters are left free. The minimisation uses the Minuit algorithm, and uncertainties are obtained from the inverse Hessian matrix. To ensure stable convergence, the fitting procedure is performed twice consecutively: the parameters obtained from the first fit are saved to a file and used as initial values for a second fit. In cases where the fit initially showed difficulty in convergence, the initial parameter values were taken from the results of the fits for the channels with opposite polarity ($K_S\pi$ down and $K\pi\pi$ down, respectively), allowing us to achieve stable convergence for all samples.

3.6 Results of the fits

The fits described in Section 3.5 are performed on the 2024 Run 3 data for each decay channel and magnet polarity. Figures 3.1–3.4 show the invariant-mass distributions. For each channel and polarity, the distributions are shown separately for D^+ and D^- candidates. In each panel, the data points are displayed with the result of the simultaneous fit overlaid (solid curve), and the signal and background components are indicated. The raw asymmetries obtained from the fits are reported in Table 3.1.

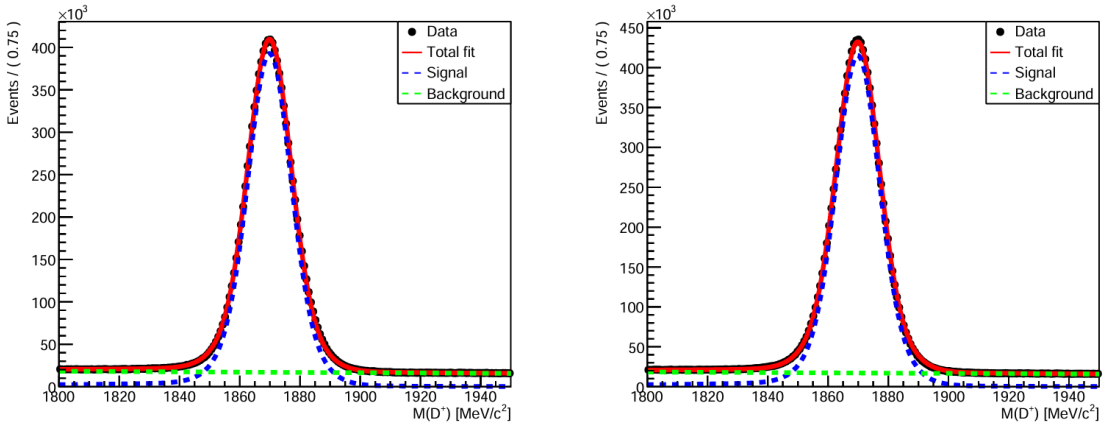

Figure 3.1: Invariant-mass distributions for the $K\pi\pi$ channel (MagUp). Left (right) panels show D^+ (D^-) candidates.

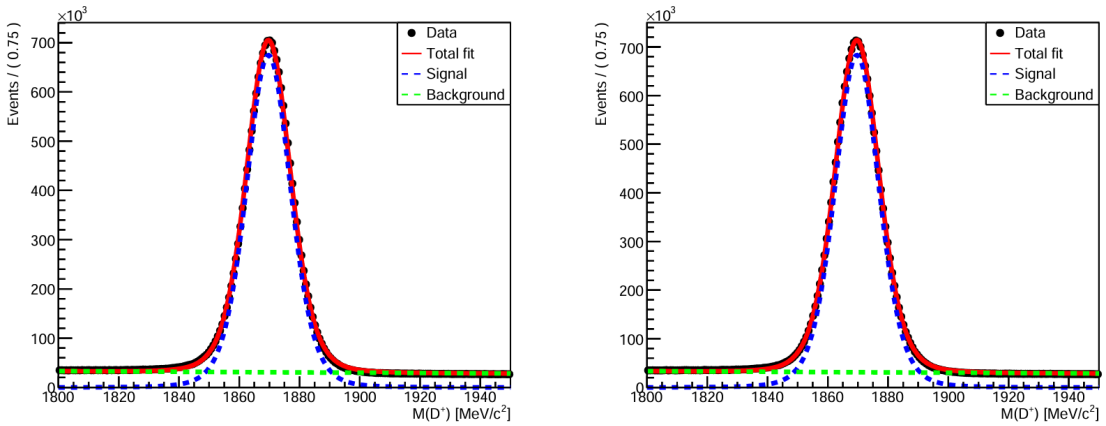

Figure 3.2: Invariant-mass distributions for the $K\pi\pi$ channel (MagDown). Left (right) panels show D^+ (D^-) candidates.

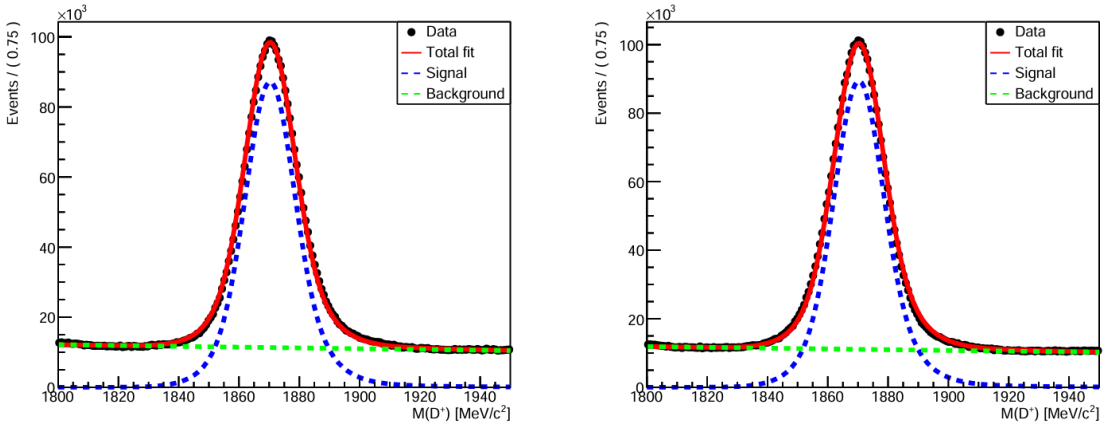

Figure 3.3: Invariant-mass distributions for the $K_S\pi$ channel (MagUp). Left (right) panels show D^+ (D^-) candidates.

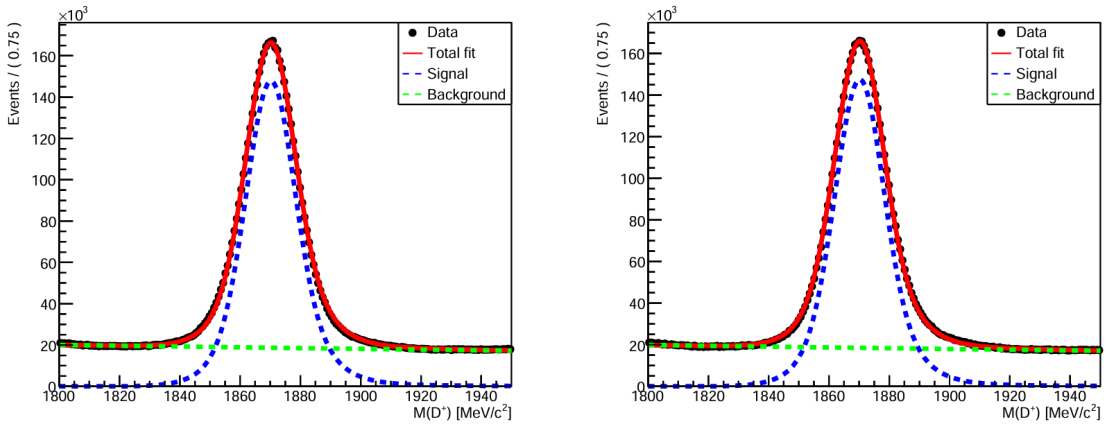

Figure 3.4: Invariant-mass distributions for the $K_S\pi$ channel (MagDown). Left (right) panels show D^+ (D^-) candidates.

Table 3.1: Raw asymmetries A_{raw} (in units of 10^{-2}) obtained from the simultaneous fits for the two decay channels and magnet polarities. Uncertainties are statistical only.

Channel	MagUp	MagDown
$K\pi\pi$	-2.78 ± 0.02	-0.26 ± 0.01
$K_S\pi$	-1.25 ± 0.04	0.09 ± 0.04

These raw asymmetries are the input to the detection asymmetry calculation described in the next section.

3.7 Combination of magnet polarities

Using the values from Table 3.1, the difference between the $K\pi\pi$ and the $K^0_S\pi$ raw asymmetries for each magnet polarity, defined as ΔA_{raw}, is computed

$$\Delta A^{\text{Up}}_{\text{raw}} = (-1.54 \pm 0.05) \cdot 10^{-2}, \tag{3.15}$$

$$\Delta A^{\text{Down}}_{\text{raw}} = (-0.36 \pm 0.04) \cdot 10^{-2}. \tag{3.16}$$

Since any left-right detector asymmetry changes sign when the magnetic field is reversed, we average the two values to cancel such effects:

$$\Delta A^{\text{avg}}_{\text{raw}} = (-0.95 \pm 0.03) \times 10^{-2}. \tag{3.17}$$

3.8 Final detection asymmetry

Finally, the known detection asymmetry of the neutral kaon is added. Since the K_S decays into a $\pi^+\pi^-$ pair, which is charge-symmetric, its detection asymmetry is zero to a good approximation: $A_{\text{det}}(K_S) = 0$. Therefore, the detection asymmetry for the $K^-\pi^+$ pair is simply the average raw asymmetry difference:

$$A_{\text{det}}(K^-\pi^+) = \Delta A^{\text{avg}}_{\text{raw}} = (-0.95 \pm 0.03) \times 10^{-2}. \tag{3.18}$$

Conclusions

The main goal of this thesis is the measurement of the detection asymmetry $A_{\text{det}}(K^-\pi^+)$. This quantity is a fundamental input for production asymmetry and CP violation measurements in the charm sector. CP asymmetries are powerful probes for physics beyond the Standard Model, while production asymmetries are essential for validating non-perturbative QCD and detector performance. The measurement is performed using part of the 2024 data collected during LHCb Run 3 at $\sqrt{s} = 13.6$ TeV. The decays $D^+ \to K^-\pi^+\pi^+$ and $D^+ \to K^0_S\pi^+$ are analysed to extract the detection asymmetry. The samples are split by magnet polarity (Up and Down). The $K^-\pi^+$ pair detection asymmetry is found to be

$$A_{\text{det}}(K^-\pi^+) = (-0.95 \pm 0.03) \times 10^{-2}.$$

With the full Run 3 statistics, the precision of this measurement will further improve, providing a valuable input for future CP violation studies within the LHCb experiment.

Bibliography

[1] C. Quigg, *Gauge Theories of the Strong, Weak, and Electromagnetic Interactions*, 2nd ed. (Princeton University Press, Princeton, 2013).

[2] D. J. Griffiths, *Introduction to Elementary Particles* (Wiley-VCH, Weinheim, 2004).

[3] M. E. Peskin and D. V. Schroeder, *An Introduction to Quantum Field Theory* (CRC Press, Boca Raton, 2019).

[4] S. Braibant, G. M. Giacomelli, and M. Spurio, *Particelle e interazioni fondamentali* (Springer, 2012).

[5] M. D. Schwartz, *Quantum Field Theory and the Standard Model* (Cambridge University Press, Cambridge, 2014).

[6] E. A. Paschos, *Electroweak Theory* (Cambridge University Press, Cambridge, 2023).

[7] S. Chatrchyan *et al.* (CMS Collaboration), "Observation of a New Boson at a Mass of 125 GeV with the CMS Experiment at the LHC," *Phys. Lett. B* **716**, 30 (2012), doi:10.1016/j.physletb.2012.08.021, arXiv:1207.7235.

[8] P. A. M. Dirac, *The Principles of Quantum Mechanics*, 4th ed. (Clarendon Press, Oxford, 1981).

[9] M. S. Sozzi, *Discrete Symmetries and CP Violation: From Experiment to Theory* (Oxford University Press, Oxford, 2008).

[10] C. S. Wu, E. Ambler, R. W. Hayward, D. D. Hoppes, and R. P. Hudson, "Experimental Test of Parity Conservation in Beta Decay," *Phys. Rev.* **105**, 1413 (1957), doi:10.1103/PhysRev.105.1413.

[11] J. H. Christenson, J. W. Cronin, V. L. Fitch, and R. Turlay, "Evidence for the 2π Decay of the K_2^0 Meson," *Phys. Rev. Lett.* **13**, 138 (1964), doi:10.1103/PhysRevLett.13.138.

[12] R. Aaij *et al.* (LHCb Collaboration), "Measurement of CP Asymmetry in $D^0 \to K_S^0 K_S^0$ Decays with Run 3 Data," *J. High Energy Phys.* **2026**, 253 (2026), doi:10.1007/JHEP02(2026)253.

[13] H. Dijkstra et al., Measurement of CP asymmetry in $D^0 \to K - K+$ and $D^0ß\pi^-\pi^+$ decays, LHCb-ANA-2013-055.

[14] C. Abellan Beteta *et al.* (LHCb Collaboration), "The LHCb Upgrade I," *JINST* **19**, P05065 (2024), doi:10.1088/1748-0221/19/05/P05065.

[15] C. Drancourt *et al.* (LHCb Collaboration), "The LHCb Detector at the LHC," *JINST* **3**, S08005 (2008), doi:10.1088/1748-0221/3/08/S08005.

[16] P. Krokovny *et al.* (LHCb Collaboration), "LHCb Detector Performance," *Int. J. Mod. Phys. A* **30**, 15300227 (2015), doi:10.1142/S0217751X15300227.

[17] L. Evans and P. Bryant, "LHC Machine," *JINST* **3**, S08001 (2008), doi:10.1088/1748-0221/3/08/S08001.

[18] ROOT Collaboration, "ROOT Data Analysis Framework," `https://root.cern`.

[19] M. Calvi *et al.*, "Minimising Event Size, Maximising Physics: Inclusive Particle Isolation for LHCb's Run 3," *Eur. Phys. J. C* **86**, 241 (2026), doi:10.1140/epjc/s10052-026-15398-5.